Inorganic Chemistry

pubs.acs.org/IC Article

Solution Processing of Spinel Nickel Cobaltite: Exfoliation Mechanism, Dispersion Stability, and Applications

Ramesh Chandra Sahoo, Priyabrata Sahoo, Manish Kumar Mohanta, Puru Jena,* and H. S. S. Ramakrishna Matte*



Cite This: Inorg. Chem. 2024, 63, 7838-7847



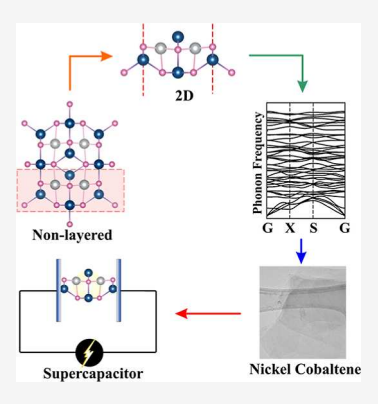
ACCESS |

Metrics & More

Article Recommendations

Supporting Information

ABSTRACT: The exfoliation of nonlayered materials to mono- or few-layers is of growing interest to realize their full potential for various applications. Nickel cobaltite (NiCo₂O₄), which has a spinel crystal structure, is one such nonlayered material with unique properties and has been utilized in a wide range of applications. Herein, NiCo₂O₄ is synthesized from NiCo₂-Layered double hydroxides using a topochemical conversion technique. Subsequently, bulk NiCo₂O₄ is exfoliated into mono- or few-layer nickel cobaltene nanosheets using liquid-phase exfoliation in various low-boiling point solvents. An analytical centrifuge technique is also utilized to understand the solute—solvent interactions by determining their dispersion stability using parameters such as the instability index and sedimentation velocity. Among the studied solvents, water/isopropyl alcohol cosolvent is found to have better dispersion stability. In addition, density functional theory calculations are carried out to understand the exfoliation mechanism. It is found that the surface termination arising from the Co–O bond needs the least energy for exfoliation. Furthermore, the obtained nickel cobaltene nanosheets are utilized as an active material for supercapacitors without any conductive additives or hinders. A solid-state states are resident to the properties of the properties and the properties and the properties are utilized as an active material for supercapacitors without any conductive additives or hinders. A solid-state states are represented in the properties and the properties and the properties are utilized as an active material for supercapacitors without any conductive additives or hinders.



active material for supercapacitors without any conductive additives or binders. A solid-state symmetric supercapacitor delivers a specific capacitance of 10.2 mF cm $^{-2}$ with robust stability, retaining \sim 98% capacitance after 4000 cycles.

INTRODUCTION

The successful exfoliation of graphene in 2004 unveiled its extraordinary properties, including superior electronic conductivity, optical transparency, mechanical rigidity, and thermal conductivity. It opened up a new era to explore the properties of various nanomaterials at the monolayer regime. 1-3 Two-dimensional (2D) materials exhibit exceptional properties due to the quantum confinement effect, surpassing their bulk counterparts.⁴⁻⁷ They offer high surface area, low diffusion path, more active sites, and superior chemical and thermal stability, and helped in enhancing the properties in various applications, including flexible electronics, catalysis, energy generation, energy storage, sensors, to name a few.⁸⁻¹⁴ This has led to the realization of a plethora of other well-known 2D materials, such as transition metal dichalcogenides, ^{15,16} hexagonal boron nitride, ¹⁷ layered double hydroxides (LDH). ^{18–20} All these 2D materials have strong in-plane and weak out-of-plane bonding, enabling them to be exfoliated into mono- or few-layers using various top-down approaches like micromechanical cleavage, ball milling, liquid-phase exfoliation (LPE), intercalation exfoliation. 15,21 Among these, LPE is a widely adopted solution processing technique for exfoliating layered 2D materials. This technique offers numerous advantages, including high processing speed, costeffectiveness, and high throughput, making it particularly appealing to researchers and industries. $^{16,21-23}$

The exploration of layered 2D materials has inspired researchers to delve into nonlayered materials as well. 22,24 For instance, hematite, ilmenite, tellurium, selenium, manganese telluride, and silicon were successfully cleaved to monoor few-layer nanosheets using solution routes. 25-30 In the case of layered materials, the weak interaction in the out-of-plane directions facilitates exfoliation, while nonlayered materials present a greater challenge due to their strong interactions in all directions. Nevertheless, the bonding anisotropy present in these materials has been effectively utilized for exfoliation. 27,31 For instance, in Si, the (111) plane exhibits the lowest bond density compared to (110), making exfoliation along (111) more favorable.³⁰ The inherent anisotropy within the crystal systems explains the exfoliation of various nonlayered materials, where the extent of anisotropy determines the aspect ratio of the exfoliated flakes. In this regard, LPE has proven highly successful in generating nanoplatelets from these materials.

In this work, spinel NiCo₂O₄ (NCO) is synthesized by employing the topochemical conversion technique. Subse-

Received: January 31, 2024 Revised: April 5, 2024 Accepted: April 5, 2024 Published: April 18, 2024





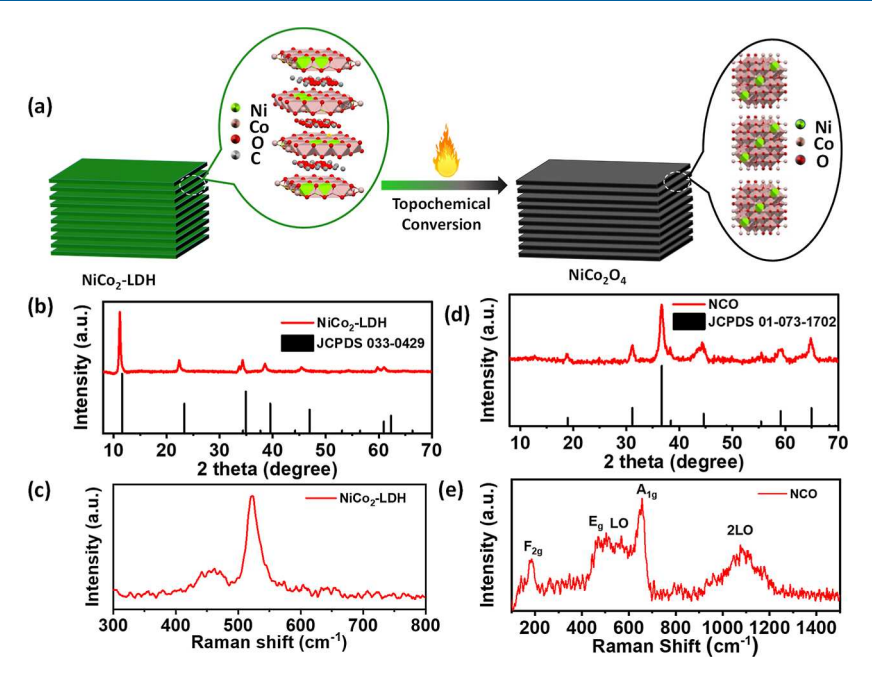


Figure 1. (a) Schematic representation of topochemical conversion of NiCo₂-LDH to NCO along with their crystal structures, (b,c) XRD, and Raman spectrum of NiCo₂-LDH, (d,e) XRD, and Raman spectrum of NCO.

quently, the obtained NCO has been successfully exfoliated into mono- or few-layer nickel cobaltene (e-NCO) nanosheets using low-boiling point water/isopropyl alcohol (WI) cosolvent. An analytical centrifuge equipped with STEP technology has been employed to assess the long-term stability of e-NCO dispersions. This technique allowed the study of dispersion behavior over an extended period within a few hours, which is critical for practical applications. Detailed theoretical calculations based on density functional theory (DFT) are probed to gain a comprehensive understanding of the exfoliation mechanism. Furthermore, the obtained e-NCO dispersions are utilized to fabricate electrodes for energy storage applications.

RESULTS AND DISCUSSION

Topochemical Conversion of NiCo₂-LDH to NCO. The topochemical synthesis technique enables the synthesis of novel materials by adding, removing, or substituting elements to or from the precursors, which preserves the structure or, at least, the morphology of the precursors used.^{32,33} Figure 1a shows the schematic representation for the conversion of NiCo₂-LDH into NiCo₂O₄ nanosheets using the topochemical synthesis technique. The crystal structure of NiCo₂-LDH consists of positively charged brucite-like metal hydroxides alternated with anions (Figure 1a). In LDH, the hydroxide ions are found at the vertices of edge-sharing octahedra, whereas the metal cations occupy the centers, joined to form infinite 2D sheets. 34,35 A detailed synthesis procedure of NiCo₂-LDH is provided in the Supporting Information. X-ray diffraction (XRD) pattern of the synthesized NiCo2-LDH is shown in Figure 1b, matching with JCPDS no. 033-0429, indicating the formation of NiCo2-LDH intercalated with carbonate anions. 19,36,37 The Raman spectrum of NiCo₂-LDH (Figure 1c) shows peaks at 480 and 522 cm⁻¹ corresponding to Ni-O and Co-O vibrational modes further support the phase formation. 38-40 The average thickness of NiCo₂-LDH is found

to be 62 nm from the Field emission scanning electron microscope (FESEM) analysis (Figure S1).

Temperature plays a crucial role in retaining the parent morphology in the topochemical conversion technique. For this, thermogravimetric analysis (TGA) has been carried out for NiCo₂-LDH within 25–900 °C with a heating rate of 5 °C/min under an O_2 environment, as shown in Figure S2. The weight loss up to 380 °C indicates the removal of water molecules and decomposition of the CO_3^{2-} ion. The negligible weight loss beyond 380 °C is attributed to the conversion of NiCo₂-LDH to NCO, as schematically represented in Figure $\frac{1}{41-44}$

This study adopts a moderate temperature of 450 $^{\circ}$ C to synthesize NCO from NiCo₂-LDH. The XRD pattern of the obtained NCO is shown in Figure 1d, matching JCPDS 01-073-1702, indicating a cubic crystal structure with a lattice constant of 8.11 Å. The presence of Raman peaks at 184, 465, 504, 654, and 1088 cm⁻¹ of NCO (Figure 1e) corresponding to F_{2g}, E_g, LO, A_{1g}, and 2LO modes, respectively, confirmed the formation of NCO. The FESEM image of the synthesized NCO is shown in Figure S3, confirming the retention of morphology after converting NiCo₂-LDH to NCO. The average lateral dimensions of the NCO bulk is \sim 1025 nm, and the size distributions of the nanosheets are shown in Figure S4, having an average thickness of 54 nm (Figure S3).

Liquid-Phase Exfoliation of NCO to e-NCO. After the successful conversion of NiCo₂-LDH to NCO, a probe sonicator is used to exfoliate NCO in various low-boiling solvents. During probe sonication, the high-power ultrasound creates alternate high-pressure (compression) and low-pressure (rarefaction). The ultrasonic waves produce tiny vacuum bubbles during the low-pressure cycle, and these bubbles progressively expand. Once they reach their maximum size, they cease to retain energy, causing the bubbles to collapse. This collapse results in the release of high-energy liquid jets, a phenomenon known as cavitation, ultimately leading to exfoliation. Various low-boiling point solvents have

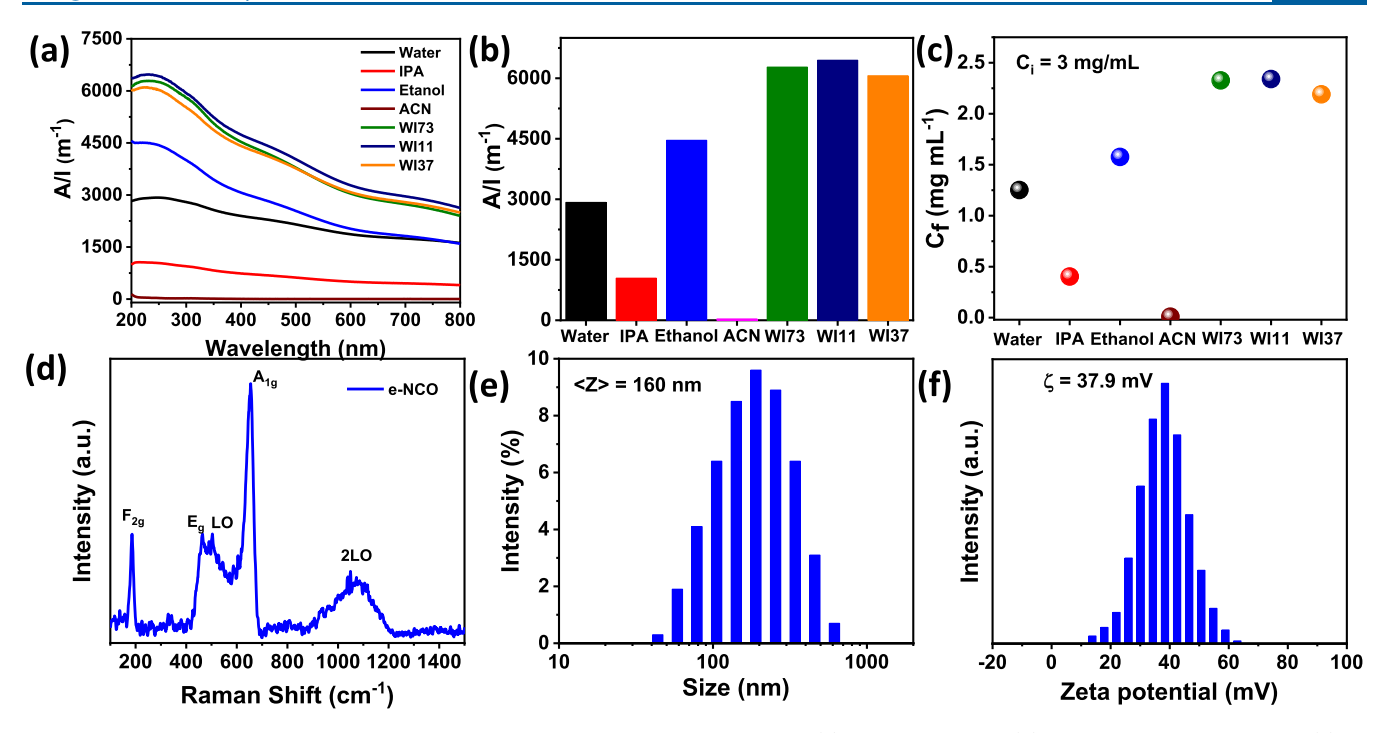


Figure 2. Characterizations of e-NCO dispersions in different low-boiling solvents. (a) UV–vis spectra, (b) A/l values at 246 nm, and (c) C_f obtained from thermogravimetry with C_i of 3 mg mL⁻¹. Characterizations of e-NCO dispersions were obtained from WI73. (d) Raman spectrum, (e) size distributions from dynamic light scattering, and (f) zeta potential.

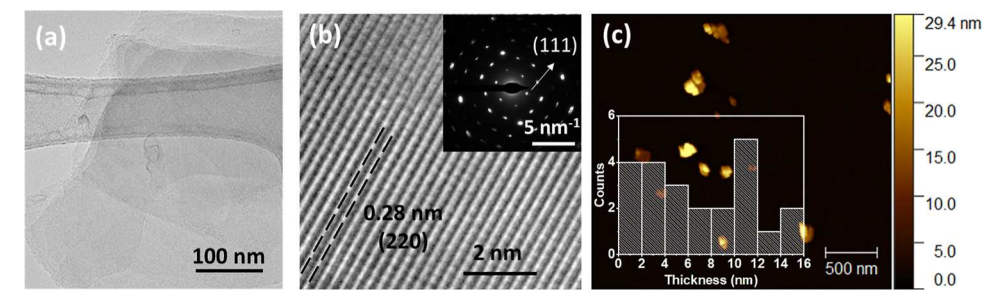


Figure 3. Microscopic characterizations of e-NCO dispersions. (a) TEM image, (b) HRTEM image with inset showing the SAED pattern, and (c) AFM image with inset showing thickness distributions.

been tested for exfoliation, and among them, dispersions in acetonitrile (ACN), acetone, and chloroform completely precipitated after 12 h due to natural sedimentations. The dispersions obtained in other low-boiling point solvents are centrifuged at 1000 rpm for 1 h, and the supernatants are collected. Subsequently, various spectroscopic and microscopic characterizations are carried out to confirm the exfoliation.

Figure 2a shows the UV-visible spectra of the dispersions obtained in various solvents. The corresponding A/l values (where A is the optical absorption and l is the cell length) at 246 nm are shown in Figure 2b. Among the different low-boiling point solvents chosen, the water/IPA cosolvent demonstrates the highest A/l values, while ACN exhibits the lowest A/l value, indicating better dispersibility of NCO in cosolvent systems. Subsequently, dispersion concentrations (C_f) in each solvent are determined by using thermogravimetric analysis (details in Supporting Information). The determined dispersion concentrations in water, IPA, ethanol, ACN, WI73, WI11, and WI37 systems are found to be 1.25, 0.40, 1.58, 0.01, 2.33, 2.34, and 2.19 mg mL⁻¹, respectively. Raman spectroscopy was carried out to confirm the phase retention after the exfoliation of NCO in WI73 cosolvent and

is shown in Figure 2d. After the exfoliation, the Raman intensity of F_{2g} peaks is enhanced and shifted from 184 to 186 cm⁻¹. Also, the presence of other Raman modes at 465, 504, 654, and 1073 cm⁻¹ corresponding to E_g LO, A_{1g}, and 2LO modes suggests the phase retention after exfoliation. The lateral size distributions obtained from dynamic light scattering (DLS) measurements of the e-NCO show an average size of 160 nm (Figure 2e). Additionally, zeta potential measurements are carried out to determine the surface charge of the e-NCO. Figure 2f shows the zeta potential distributions of e-NCO in WI73 cosolvent with an average zeta potential of +37.9 mV. A positive charge on the surface of the exfoliated nanosheets helps in stabilizing the dispersions in the water/IPA cosolvent.

Furthermore, microscopic characterizations are also carried out to confirm the exfoliation. The low-magnification transmission electron microscope (TEM) image of e-NCO in WI73, shows nanosheet morphology (Figure 3a). The high-resolution TEM (HRTEM) image (Figure 3b) reveals the lattice fringes with a *d*-spacing of 0.28 nm, corresponding to the (220) plane of NCO, in agreement with the XRD results (JPCDS 01-073-1702). The highly crystalline nature of e-NCO with a spinel crystal structure is confirmed by the SAED

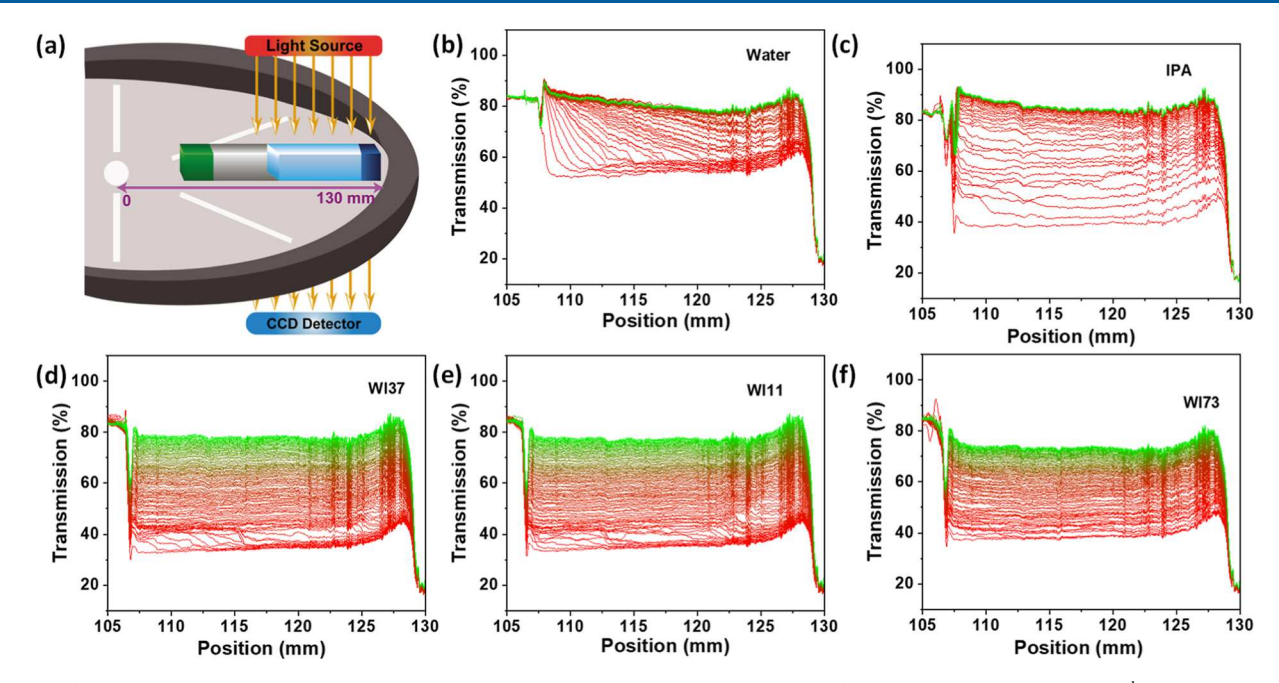


Figure 4. (a) Schematic representation of a typical dispersion analyzer setup employed, (b-f) transmission profiles (each 5th profile) of e-NCO dispersions in various solvents recorded at a centrifugation speed of 2000 rpm.

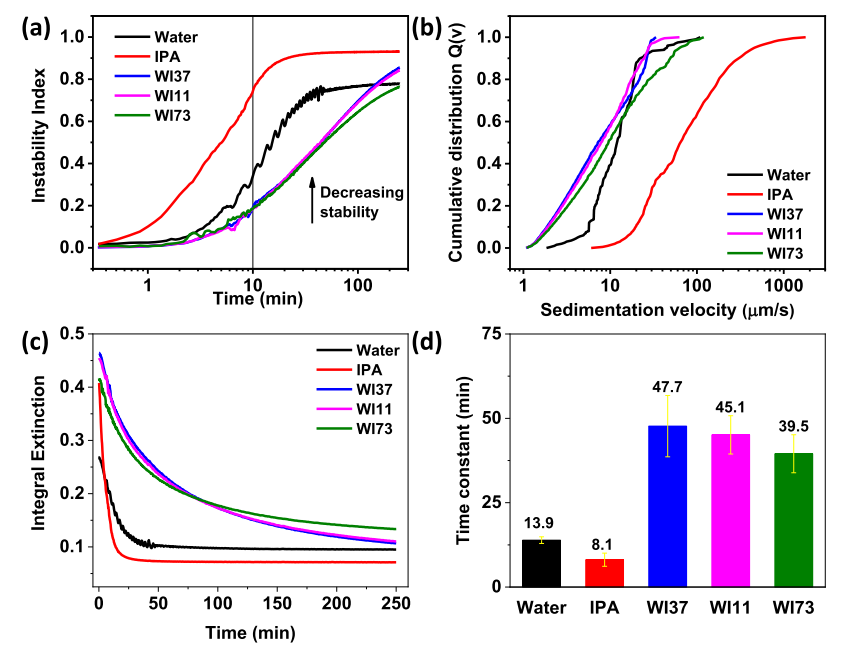


Figure 5. Stability analysis of e-NCO dispersions. (a) Change in instability index with time. (b) Sedimentation velocity distribution plot. (c) Variation of integral extinction with time. (d) Calculated decay time constants after fitting the integral extinction.

pattern, shown in the inset of Figure 3b. Moreover, the atomic force microscope (AFM) micrograph, shown in Figure 3c, indicates an average thickness of 7–8 nm (inset of Figure 3c).

Accelerated Stability Studies of e-NCO Dispersions. After comprehensive spectroscopic and microscopic characterizations of e-NCO in water/IPA cosolvent systems, the stability of the dispersions is analyzed employing an analytical centrifuge. Understanding the dispersion stability is crucial not only to realize the solute—solvent interactions but also to utilize them in various applications. In this accelerated measurement technique, transmission profiles are recorded at specific time intervals under higher gravitational acceleration,

enabling the determination of the sedimentation velocity, instability index, and integral extinction. The experimental setup is schematically shown in Figure 4a, where the distance between the center position of the rotor and the bottom of the cuvette is 130 mm. As time progresses, the dispersed nanosheets move from their initial position to the bottom of the cell due to the centrifugal force, leading to an increase in light transmission through the dispersion. By monitoring the change in transmitted light intensity over time across the spatial length of the cuvette, the sedimentation kinetics of the dispersion can be understood. Among the recorded profiles, every fifth profile is plotted and is shown in Figure 4b—f for

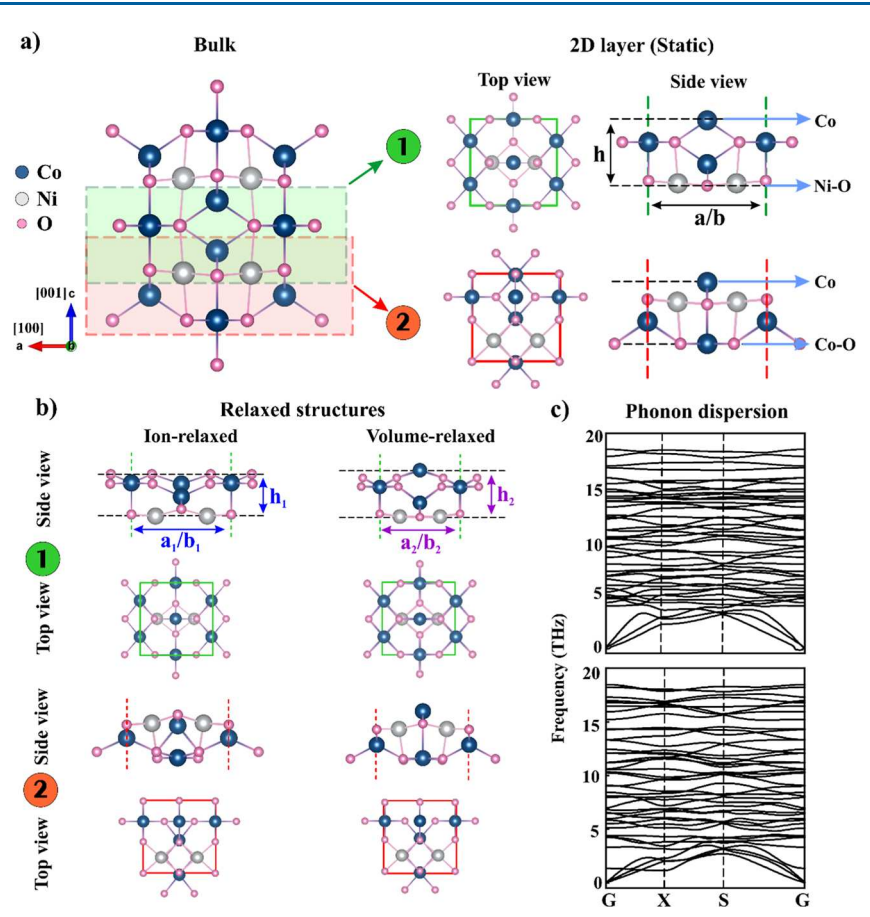


Figure 6. (a) Schematic illustration of computationally designed different surface-terminated 2D structures of NiCo₂O₄ from its bulk; (a/b) inplane lattice constants and (h) slab height. (b) Top and side view of optimized geometries. (c) Phonon dispersion of the 2D relaxed structures plotted along high symmetry directions of rectangular Brillouin zone; G (0,0,0), X (0.5,0,0), S (0.5,0.5,0), and G (0,0,0).

various solvent systems. The first and last transmission profiles are shown in red and green, respectively, while a gradient of these colors represents the progress of the measurements.

For accessing the stability of e-NCO dispersions in different solvents, exfoliation has been carried out in water, IPA, and water/IPA cosolvent systems with water to IPA ratios as 3:7, 1:1, and 7:3 with an initial concentration of 0.2 mg mL⁻¹. A qualitative evaluation of dispersion concentrations was performed by examining their transmission profiles, where lower transmission values indicate higher dispersion concentrations. As shown in Figure 4b-f, the initial transmission values of e-NCO dispersions in water, IPA, WI37, WI11, and WI73 are found to be \sim 52, 38, 33, 34, and 38%, respectively. suggesting poorer exfoliation yield in water compared to other solvents. Over the course of the measurement, the stability of dispersions can be evaluated qualitatively by analyzing the separation between consecutive transmission profiles. The separation between the first two consecutive profiles at 115 mm position for IPA, water, WI37, WI11, and WI73 solvents are found to be 2.8, 1.1, 0.4, 0.4, and 0.3%, respectively. A larger separation in the case of e-NCO dispersion obtained in IPA indicates the poorer dispersion stability (Figure 4c).⁴⁷ In contrast, a narrower spacing between the profiles is observed in the case of e-NCO dispersion in water/IPA cosolvent systems, implying better stability.

To further understand the stability of the e-NCO dispersions, the instability index, which is defined as the change in transmission at any time divided by the maximum

transmission change possible, is determined.⁴⁸ When the dispersed phase gets separated from the continuous phase, the instability index increases, and therefore, a higher value of the instability index signifies less dispersion stability. The instability indices of water, IPA, WI37, WI11, and WI73 are found to be 0.33, 0.73, 0.19, 0.18, and 0.18, respectively, after 10 min of measurement (Figure 5a). Further, the sedimentation velocities are also determined from the recorded transmission profiles and are plotted as a cumulative distribution in Figure 5b. Median sedimentation velocities of e-NCO dispersions in water, IPA, WI37, WI11, and WI73 are found to be 11.9, 42.4, 7.8, 8.2, and 10.3 μ m/s, respectively (Figure S5). It is noted that the sedimentation velocities are spanned over a broad region as expected from liquid-phase exfoliated dispersions having nanosheets of broad size distributions as shown in Figure 5b. 49

In addition to the instability index and sedimentation velocity, the decay time constant is another valuable parameter for gaining further insights into the stability of e-NCO dispersions. For this, transmission profiles are converted into extinction profiles according to Beer-lambert law and shown in Figure S6a—e. From these extinction profiles, integral extinction (IE) values are calculated and are shown in Figure Sc. IE plot is interpreted with the following first-order exponential decay equation 50

$$A(t) = A_0 + A_1 \times e^{-t/\tau} \tag{1}$$

Table 1. Calculated Lattice Parameters (Unit Å) of Designed NiCo₂O₄ in Their Static and Optimized Geometries and Their Relative Percentage Change $\left(\frac{a_{2D}-a_{bulk}}{a_{bulk}}\times 100\right)$ Relative to the Bulk

systems	static		ionic-relaxed structures $(a_1 = a; b_1 = b)$		relative % change	volume-relaxed structures		relative % change		
	а	ь	h	h_1	h	a_2	b_2	h_2	а	ь
NCO-1	5.81	5.82	3.24	2.44	-24.7	5.53	5.46	3.22	-48.2	-61.85
NCO-2			2.99	2.46	-18.4	5.69	5.58	2.99	-20.7	-41.20

where A(t) and A_0 represent the instantaneous and equilibrium IE, respectively. A significant part of IE, which decays over time with sedimentation time constant τ is represented by A_1 . The fitted IE plots of all of the dispersions are shown in Figure S7. The average decay time constants and sedimentation constants of three independent measurements are represented in Figure 5d. Decay time constants in water, IPA, WI37, WI11, and WI73 are observed to be 13.9, 8.1, 47.7, 45.1, and 39.5 min, respectively, suggesting dispersions in cosolvents are more stable compared to others, corroborating the observations with instability index and sedimentation velocity studies. It is to be noted that the time constant represented here is at a gravitational acceleration of ~514 g. Assuming the linear relationship between sedimentation velocity and relative centrifugal acceleration (RCA), sedimentation time constants can be extrapolated at 1 g by multiplying it with RCA.⁵¹ It can be concluded that all three cosolvent systems are found to be equally good for both exfoliation and stabilization when compared to their individual counterparts. However, it is to be noted that IPA is found to have good exfoliation efficiency but rather poor dispersion stability.

Computational Studies. A comprehensive computational study based on DFT calculations has been conducted to shed light on the stability of free-standing nickel cobaltene monolayers and the exfoliation energy required for different surface termination. For this, two 2D structures of NCO having different surface terminations are sliced from its bulk orthorhombic crystal structure (space group Imma)⁵² perpendicular to the [001] direction. These are indicated by green (marked as 1) and red (marked as 2) colors and are schematically illustrated in Figure 6. The difference in surface terminations is shown in Figure 6a. Each unit cell contains 14 atoms consisting of two Ni atoms, four Co atoms, and eight O atoms. The geometries of the 2D structures are subjected to both ionic coordinates and volume relaxation. Significant atomic rearrangement is observed in both cases and their final geometries are plotted in Figure 6b. The lattice constants before and after structural relaxations are given in Table 1 for comparison, and their relative percentage change is indicated. These results lead us to the following conclusions: In the case of ionic relaxations, the structure is compressed vertically to compensate for the dangling bonds along the z-direction. With regard to volume relaxation, the system tries to retain the initial structure, and hence, in-plane lattice parameters are compressed up to ~60%, which implies stronger bonds are formed in free-standing 2D structures. For example, the bond length of Ni-O (2.01 Å) in static geometry is reduced to 1.85 Å in volume-relaxed structure, as indicated in Figure S8. To check the dynamical stability of the freely designed 2D structure, the phonon dispersions are plotted in Figure 6c. The positive frequencies of all vibrational modes confirm their dynamical stability. It is clear from Figure S9 that the exfoliation energy of the Ni-O-terminated surface will be higher compared to the

Co-O terminated surface. Since more energy is required to break the short adjacent bonds in bulk structure, Co-O terminated 2D NCO is more likely to be obtained in the experiment. The exfoliation energies for both static and relaxed structures are theoretically calculated for NCO-1 and NCO-2, as shown in Table 2. More details about the theoretical

Table 2. Calculated Exfoliation Energies of Computationally Designed NiCo₂O₄ Using the GGA + U Method and Other Materials for Comparison

systems	exfoliation energy (meV/Å $^2)$			
	static	relaxed structure		
NCO-1 (this work)	236.7	130.1		
NCO-2 (this work)	173.7	123.7		
$Al_2S_3^{53}$	196	47		
graphene ^{54,55}	20			
X_2O_3 (X = Al, Cr, Fe, Ga, In, Rh, Ti, V) ⁵⁶	100-200			

methods used in this work are given in Supporting Information. The DFT calculations carried out here are to study the cleavage surface and have not been extended to understand the solute—solvent interactions.

Applications of e-NCO as Active Materials for **Supercapacitors.** The exfoliated nanosheets are utilized for supercapacitor applications after the successful exfoliation of NCO to nickel cobaltene. The dispersions of NCO in WI73 have been used for fabricating supercapacitors by depositing them on CC in an area of 1 cm \times 1 cm using the spray coating technique (details in Supporting Information), as the stability and exfoliation efficiency of all the cosolvent systems (WI73/ WI11/WI37) are comparable. The thickness of the films is optimized by changing the volume of the e-NCO dispersions deposited on CC, starting from 1 to 7 mL, and the corresponding films are named as e-NCO-1 to e-NCO-7, respectively. Figure S10a shows the cyclic voltammograms (CV) of bare CC and e-NCO-2 at a scan rate of 5 mV s⁻¹. The CC shows negligible capacity contributions compared with the e-NCO-2 film. The CV curve of e-NCO-2 shows two distinct redox peaks may be arising due to the following redox reactions 57,58

$$NiCo_2O_4 + H_2O \leftrightarrow NiOOH + 2CoOOH + 2e^-$$
 (2)

$$MOOH + OH^{-} \leftrightarrow MO_2 + H_2O + e^{-}$$
 (3)

where M represents Ni and Co ions. The observed distinct oxidation peaks in the case of e-NCO-2 may be due to the facile transfer of electrons. Figure S10b shows the CV of e-NCO-1 to e-NCO-7 films, and it is observed that upon increasing the thickness of the film, the area under the CV curves increases, suggesting an enhancement in the charge storage capacity. It is to be noted that the oxidation peaks shifted slightly to higher potential upon increasing the loading

 Inorganic Chemistry
 pubs.acs.org/IC
 Article

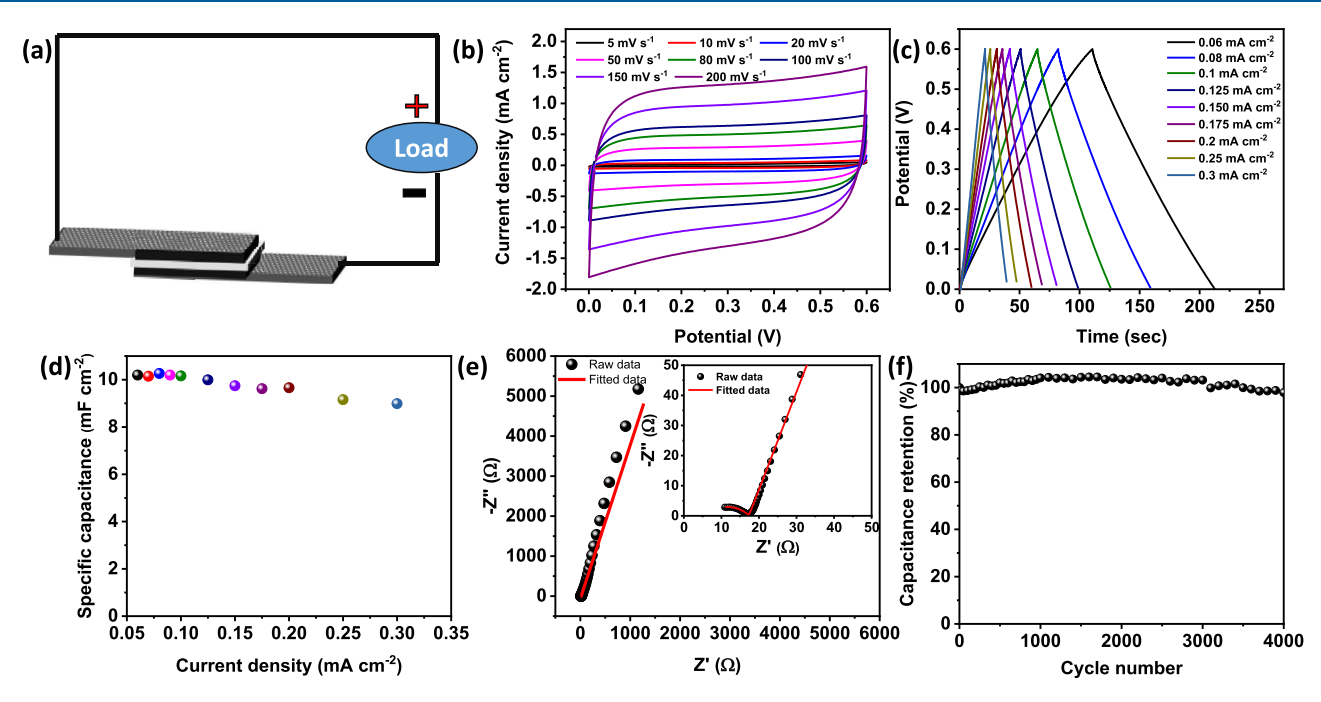


Figure 7. (a) Schematic representation of the symmetric solid-state supercapacitor, (b) CV, (c) GCD, (d) variation of areal capacitance with current density, (e) EIS, and (f) stability of the symmetric e-NCO solid-state supercapacitor with KOH as the gel electrolyte.

of e-NCO. The areal capacity is calculated from CV using the following equation.⁵⁹

$$Q_{s} = \frac{\int I(V) \, dV}{A\nu} \tag{4}$$

where $Q_{s,\nu} \int I(V) dV$, A, and ν represent the specific capacity (C cm⁻²), the absolute area under the CV curve, the area of active material coated on CC (1 cm² here), and the scan rate (V s⁻¹), respectively. Figure S10c shows the specific capacity of e-NCO-1 to e-NCO-7 films at a scan rate of 5 mV s⁻¹. It is observed that the specific capacity increases from e-NCO-1 to e-NCO-7. For further study, the e-NCO-7 film is considered as it provides maximum capacity. Figure S10d shows the scanrate-dependent charge storage performance at a scan rate of 5-50 mV s⁻¹. Upon increasing the scan rate, the potential difference between the oxidation and reduction peaks is found to increase and may be attributed to the polarization of the electrode at high scan rates.⁵⁸ Along with that, the merging of two distinct oxidation peaks is also observed at a high scan rate. The variation of areal capacity with scan rate is shown in Figure S10e. As expected, the areal capacity decreases with the increase in scan rates.⁵⁸ Figure S10f shows the galvanostatic charge-discharge (GCD) curves of e-NCO-7 film at different current densities. The nonlinear behavior of the chargedischarge curve suggests the pseudocapacitive nature of the electrode.

To further understand the charge storage dynamics of e-NCO, the staircase potentio-electrochemical impedance spectroscopy technique, a complementary technique to CV is utilized in the potential window of 0–0.6 V. For this, a step potential of 25 mV was applied for 600 s, followed by measuring the impedance over the frequency range of 10 mHz to 100 kHz with an AC amplitude of 10 mV (10 points per decade in log scale). By approximating the electrode/electrolyte interface with an equivalent circuit comprising R and C in series, the real part of capacitance (C') has been

estimated in the frequency range of 10 Hz to 10 mHz. 20,60,61 The real capacitance (C') is calculated using the following equations 62

$$C' = \frac{-Z''}{2\pi f |Z|^2} \tag{5}$$

where Z' and |Z| represent the real and absolute value of the impedance.

The phase angle
$$(\phi)$$
 is given by: $\phi = \tan^{-1} \left(\frac{Z'(\omega)}{Z''(\omega)} \right)$ (6)

The variation of C' with frequency and applied potential is shown in Figure S11a. The 3D capacitance mapping shows a sharp peak around 0.40 V versus Hg/HgO and another peak at 0.48 V with a gradual decrease in capacitance on either side of the potential, suggesting the pseudocapacitive behavior. From 3D EIS, two distinct oxidation peaks of e-NCO are observed, similar to CV curves, suggesting a two-step oxidation. This phenomenon is further confirmed by the variation of the phase angle with frequency and the applied potential, which is shown in Figure S11b. The phase angle is almost constant for the applied potential in the range of $0-0.30 \text{ V} (\sim 79^{\circ})$. A gradual decrease in phase angle shows two dips around 0.40 and 0.48 V versus Hg/HgO, which is attributed to the semi-infinite diffusion mechanism, and the phase angle further increases gradually. However, a sudden decrease in phase angle beyond 0.5 V suggests the dominance of resistive behavior. 60 At a lower voltage, the phase angle is almost constant and close to 79° at lower frequencies, suggesting the dominance of the double-layer capacitance.

Symmetric Solid-State Supercapacitor Performance of e-NCO. Furthermore, a solid-state symmetric supercapacitor is fabricated, and the schematic is shown in Figure 7a, with a PVA/KOH gel as the electrolyte. Figure 7b shows the corresponding CV curves at different scan rates. The CV curves show nearly rectangular behavior in the solid-state

electrolyte. The GCD curves shown in Figure 7c, at different current densities are nearly linear. The specific capacitance in two-electrode configuration has been calculated using the following equation⁶³

$$C_{\rm s} = \frac{I\Delta t}{A(V_2 - V_1)} \tag{7}$$

where $C_{\rm s}$ represents the specific capacitance (F cm⁻²), I/A represents the current density (A cm⁻²), Δt represents the discharge time (s), and (V_2-V_1) represents the potential window (V). The variation of areal capacitance with different current densities is shown in Figure 7d. Further, the Nyquist plot shown in Figure 7e has an $R_{\rm s}$ of 5.35 Ω and $R_{\rm ct}$ of 12 Ω , suggesting good contact between the solid-state electrolyte and e-NCO-7 film, and the phase angle reached a value of ~78° at a lower frequency, suggesting a capacitive behavior (Figure S12). The Randles equivalent circuit elements and the corresponding values are provided in Figure S13. The symmetric solid-state device also shows excellent cycling stability, with a capacity retention of 98% after 4000 cycles (Figure 7f).

CONCLUSIONS

In conclusion, the topochemical synthesis route has been employed to obtain NCO (54 nm thick) with a layered structure from its parent precursor NiCo₂-LDH. Subsequently, liquid-phase exfoliation of NCO has led to the formation of mono- or few-layers of nickel cobaltene nanosheets of 7-8 nm thickness. Comprehensive characterization techniques have confirmed the successful exfoliation of NCO and provided insights into the e-NCO dispersion sedimentation stability. Detailed theoretical calculations have been carried out to explore the exfoliation mechanism, focusing on different surface-terminated 2D NCO structures from the (001) plane of the bulk nonlayered structure. Although these monolayers are dynamically stable, the Co-O surface-terminated structure requires the least exfoliation energy since the adjacent bonds with other layers are weaker than those of the Ni-O surfaceterminated structure. The obtained e-NCO has been utilized for energy storage applications, exhibiting an areal capacity of 358 mC cm⁻² at 5 mV s⁻¹ in a three-electrode configuration, possibly due to the facile electron transfer. Additionally, a solid-state supercapacitor is fabricated. In general, direct exfoliation of nonlayered materials leads to relatively lower dispersion concentration due to the higher exfoliation energy of the crystal planes. However, the approach employed in this study, combining topochemical conversion and successive exfoliation, has proven to be an effective strategy for producing nanosheets of a nonlayered material. This approach provides a sustainable and scalable solution for synthesizing high-quality nanosheets of other nonlayered nanomaterials.

ASSOCIATED CONTENT

Supporting Information

The Supporting Information is available free of charge at https://pubs.acs.org/doi/10.1021/acs.inorgchem.4c00430.

Computational details, experimental details, TGA, FESEM image with size distribution, median sedimentation velocities, extinction profiles, fitting of the integral extinction, bond length of static and optimized geometry, bond length needs to be broken for exfoliation, electrochemical performances of nickel

cobaltene, 3D EIS, Bode plot of solid-state supercapacitor and Randles equivalent circuit (PDF)

AUTHOR INFORMATION

Corresponding Authors

H. S. S. Ramakrishna Matte — Energy Materials Laboratory, Centre for Nano and Soft Matter Sciences, Bangalore 562162, India; Manipal Academy of Higher Education (MAHE), Manipal 576104, India; orcid.org/0000-0001-8279-8447; Email: matte@cens.res.in, krishnamatte@gmail.com

Puru Jena — Department of Physics, Virginia Commonwealth University, Richmond, Virginia 23284, United States; orcid.org/0000-0002-2316-859X; Email: pjena@vcu.edu

Authors

Ramesh Chandra Sahoo — Energy Materials Laboratory, Centre for Nano and Soft Matter Sciences, Bangalore 562162, India; Manipal Academy of Higher Education (MAHE), Manipal 576104, India; orcid.org/0000-0001-5370-0965

Priyabrata Sahoo — Energy Materials Laboratory, Centre for Nano and Soft Matter Sciences, Bangalore 562162, India; Manipal Academy of Higher Education (MAHE), Manipal 576104, India

Manish Kumar Mohanta — Department of Physics, Virginia Commonwealth University, Richmond, Virginia 23284, United States; orcid.org/0000-0002-5476-8336

Complete contact information is available at: https://pubs.acs.org/10.1021/acs.inorgchem.4c00430

Author Contributions

P.S. and M.K.M. contributed equally. H.S.S.R.M. conceived the idea. R.C.S. has carried out the synthesis, characterizations, and supercapacitors study under the supervision of H.S.S.R.M. P.S. has carried out the dispersion analysis under the supervision of H.S.S.R.M. M.K.M. have carried out the computational simulations under the supervision of P.J. H.S.S.R.M. and P.J. monitored the execution of the project. The manuscript was written through the contributions of all authors. All authors have given approval to the final version of the manuscript.

Notes

The authors declare no competing financial interest.

ACKNOWLEDGMENTS

H.S.S.R.M. acknowledges Core Research Grant SERB, DST with grant number CRG/2023/005600 for financial support. R.C.S. acknowledges the Council of Scientific & Industrial Research (CSIR), New Delhi, for SRF fellowship (09/ 1243(0003)/2019-EMR-I). P.S. acknowledges UGC, New Delhi for fellowship (ref no. 1396/CSIR-UGC NET JUNE 2017. The authors acknowledge Central Research Facilities (CRF), Centre for Nano and Soft Matter Sciences, Bengaluru for carrying out different experimental work and characterizations. P.J. acknowledges partial support from the U.S. Department of Energy, Office of Basic Energy Sciences, Division of Materials Sciences and Engineering under Award no. DE-FG02-96ER45579. The authors M.K.M. and P.J. acknowledge computational resources provided by the National Energy Research Scientific Computing Center supported by the Office of Science of the U.S. Department of Energy

under Contract no. DE-AC02-05CH11231 and the High-Performance Research Computing (HPRC) core facility at Virginia Commonwealth University.

ABBREVIATIONS

NCO, NiCo₂O₄; e-NCO, nickel cobaltene nanosheets; LDH, layered double hydroxides; LPE, liquid-phase exfoliation; DFT, density functional theory; XRD, X-ray diffraction; FESEM, field emission scanning electron microscope; TGA, thermogravimetric analysis; TEM, transmission electron microscope; AFM, atomic force microscope; IE, integral extinction; RCA, relative centrifugal acceleration; CC, carbon cloth; e-NCO-1, nickel cobaltene nanosheets dispersion of volume 1 mL; ACN, acetonitrile; IPA, isopropyl alcohol; WI73, water/IPA (7:3) cosolvent; WI11, water/IPA (1:1) cosolvent; WI37, water/IPA (3:7) cosolvent; CV, cyclic voltammetry; GCD, galvanostatic charge—discharge; EIS, electrochemical impedance spectroscopy

REFERENCES

- (1) Novoselov, K. S.; Geim, A. K.; Morozov, S. V.; Jiang, D.; Zhang, Y.; Dubonos, S. V.; Grigorieva, I. V.; Firsov, A. A. Electric field effect in atomically thin carbon films. *Science* **2004**, *306*, 666–669.
- (2) Bonaccorso, F.; Lombardo, A.; Hasan, T.; Sun, Z.; Colombo, L.; Ferrari, A. C. Production and processing of graphene and 2D crystals. *Mater. Today* **2012**, *15*, 564–589.
- (3) Matte, H. S. S. R.; Subrahmanyam, K. S.; Rao, C. N. R. Synthetic Aspects and Selected Properties of Graphene. *Nanomater. Nanotechnol.* **2011**, *1*, 5.
- (4) Mohanta, M. K.; Rawat, A.; Jena, N.; Dimple; Ahammed, R.; De Sarkar, A. Interfacing Boron Monophosphide with Molybdenum Disulfide for an Ultrahigh Performance in Thermoelectrics, Two-Dimensional Excitonic Solar Cells, and Nanopiezotronics. *ACS Appl. Mater. Interfaces* **2020**, *12*, 3114–3126.
- (5) Mohanta, M. K.; De Sarkar, A. Coupled spin and valley polarization in monolayer HfN₂ and valley-contrasting physics at the HfN₂-WSe₂ interface. *Phys. Rev. B* **2020**, *102*, 125414.
- (6) Mohanta, M. K.; Is, F.; Kishore, A.; De Sarkar, A. Spin-Current Modulation in Hexagonal Buckled ZnTe and CdTe Monolayers for Self-Powered Flexible-Piezo-Spintronic Devices. *ACS Appl. Mater. Interfaces* **2021**, *13*, 40872–40879.
- (7) Mohanta, M. K.; Kishore, A.; De Sarkar, A. Two-dimensional ultrathin van der Waals heterostructures of indium selenide and boron monophosphide for superfast nanoelectronics, excitonic solar cells, and digital data storage devices. *Nanotechnology* **2020**, *31*, 495208.
- (8) Sahoo, R. C.; Lu, H.; Garg, D.; Yin, Z.; Matte, H. S. S. R. Bandgap engineered g- C_3N_4 and its graphene composites for stable photoreduction of CO_2 to methanol. *Carbon* **2022**, *192*, 101–108.
- (9) Low, J.; Cao, S.; Yu, J.; Wageh, S. Two-dimensional layered composite photocatalysts. *Chem. Commun.* **2014**, *50*, 10768–10777.
- (10) Akinwande, D.; Petrone, N.; Hone, J. Two-dimensional flexible nanoelectronics. *Nat. Commun.* **2014**, *5*, 5678.
- (11) Ahmed, A.; Sharma, S.; Adak, B.; Hossain, M. M.; LaChance, A. M.; Mukhopadhyay, S.; Sun, L. Two-dimensional MXenes: New frontier of wearable and flexible electronics. *InfoMat* **2022**, 4, No. e12295.
- (12) Xue, Y.; Zhang, Q.; Wang, W.; Cao, H.; Yang, Q.; Fu, L. Opening two-dimensional materials for energy conversion and storage: a concept. *Adv. Energy Mater.* **2017**, *7*, 1602684.
- (13) Rohaizad, N.; Mayorga-Martinez, C. C.; Fojtů, M.; Latiff, N. M.; Pumera, M. Two-dimensional materials in biomedical, biosensing and sensing applications. *Chem. Soc. Rev.* **2021**, *50*, 619–657.
- (14) Rao, C.; Matte, H. S. S. R.; Subrahmanyam, K. Synthesis and selected properties of graphene and graphene mimics. *Acc. Chem. Res.* **2013**, *46*, 149–159.
- (15) Halim, U.; Zheng, C. R.; Chen, Y.; Lin, Z.; Jiang, S.; Cheng, R.; Huang, Y.; Duan, X. A rational design of cosolvent exfoliation of

- layered materials by directly probing liquid-solid interaction. *Nat. Commun.* **2013**, *4*, 2213.
- (16) Lobo, K.; Trivedi, S.; Matte, H. S. S. R. Highly concentrated and stabilizer-free transition-metal dichalcogenide dispersions in low-boiling point solvent for flexible electronics. *Nanoscale* **2019**, *11*, 10746–10755.
- (17) Gupta, B.; Matte, H. S. S. R. Solution-Processed Layered Hexagonal Boron Nitride Dielectrics: A Route toward Fabrication of High Performance Flexible Devices. ACS Appl. Electron. Mater. 2019, 1, 2130–2139.
- (18) Moolayadukkam, S.; Thomas, S.; Sahoo, R. C.; Lee, C. H.; Lee, S. U.; Matte, H. S. S. R. Role of transition metals in layered double hydroxides for differentiating the oxygen evolution and nonenzymatic glucose sensing. ACS Appl. Mater. Interfaces 2020, 12, 6193–6204.
- (19) Sahoo, R. C.; Moolayadukkam, S.; Thomas, S.; Asle Zaeem, M.; Matte, H. S. S. R. Solution processed Ni₂Co layered double hydroxides for high performance electrochemical sensors. *Appl. Surf. Sci.* **2021**, *541*, 148270.
- (20) Sahoo, R. C.; Moolayadukkam, S.; Seok, J. H.; Lee, S. U.; Matte, H. S. S. R. Enhanced charge storage capacity and high rate capabilities of Ni₂Co-layered double hydroxides/expanded-graphite composites as anodes for Li-ion batteries. *J. Mater. Chem. A* **2023**, *11*, 7142–7151.
- (21) Nicolosi, V.; Chhowalla, M.; Kanatzidis, M. G.; Strano, M. S.; Coleman, J. N. Liquid exfoliation of layered materials. *Science* **2013**, 340, 1226419.
- (22) Kaur, H.; Coleman, J. N. Liquid-phase Exfoliation of Nonlayered non-van der Waals Crystals into Nanoplatelets. *Adv. Mater.* **2022**, *34*, 2202164.
- (23) Sahoo, P.; Gupta, B.; Sahoo, R. C.; Vankayala, K.; Matte, H. S. S. R. Solution Processing of Topochemically Converted Layered WO₃ for Multifunctional Applications. *Chem.—Eur. J.* **2021**, *27*, 11326–11334.
- (24) Tao, P.; Yao, S.; Liu, F.; Wang, B.; Huang, F.; Wang, M. Recent advances in exfoliation techniques of layered and non-layered materials for energy conversion and storage. *J. Mater. Chem. A* **2019**, *7*, 23512–23536.
- (25) Puthirath Balan, A.; Radhakrishnan, S.; Woellner, C. F.; Sinha, S. K.; Deng, L.; Reyes, C. d. l.; Rao, B. M.; Paulose, M.; Neupane, R.; Apte, A.; et al. Exfoliation of a non-van der Waals material from iron ore hematite. *Nat. Nanotechnol.* **2018**, *13*, 602–609.
- (26) Puthirath Balan, A.; Radhakrishnan, S.; Kumar, R.; Neupane, R.; Sinha, S. K.; Deng, L.; de los Reyes, C. A.; Apte, A.; Rao, B. M.; Paulose, M.; Vajtai, R.; Chu, C. W.; Costin, G.; Martí, A. A.; Varghese, O. K.; Singh, A. K.; Tiwary, C. S.; Anantharaman, M. R.; Ajayan, P. M. A Non-van der Waals Two-Dimensional Material from Natural Titanium Mineral Ore Ilmenite. *Chem. Mater.* 2018, 30, 5923–5931.
- (27) Xie, Z.; Xing, C.; Huang, W.; Fan, T.; Li, Z.; Zhao, J.; Xiang, Y.; Guo, Z.; Li, J.; Yang, Z.; et al. Ultrathin 2D nonlayered tellurium nanosheets: facile liquid-phase exfoliation, characterization, and photoresponse with high performance and enhanced stability. *Adv. Funct. Mater.* **2018**, 28, 1705833.
- (28) Xing, C.; Xie, Z.; Liang, Z.; Liang, W.; Fan, T.; Ponraj, J. S.; Dhanabalan, S. C.; Fan, D.; Zhang, H. 2D nonlayered selenium nanosheets: facile synthesis, photoluminescence, and ultrafast photonics. *Adv. Opt. Mater.* **2017**, *5*, 1700884.
- (29) Puthirath Balan, A.; Radhakrishnan, S.; Neupane, R.; Yazdi, S.; Deng, L.; A. de los Reyes, C.; Apte, A.; B. Puthirath, A.; Rao, B. M.; Paulose, M.; Vajtai, R.; Chu, C.-W.; Martí, A. A.; Varghese, O. K.; Tiwary, C. S.; Anantharaman, M. R.; Ajayan, P. M. Magnetic Properties and Photocatalytic Applications of 2D Sheets of Nonlayered Manganese Telluride by Liquid Exfoliation. ACS Appl. Nano Mater. 2018, 1, 6427–6434.
- (30) Wang, Y.; Cai, R.; Zhang, J.; Cui, J.; Qin, Y.; Zhang, Y.; Wu, J.; Chatterjee, K.; Ajayan, P. M.; Wu, Y. Directly Exfoliated Ultrathin Silicon Nanosheets for Enhanced Photocatalytic Hydrogen Production. *J. Phys. Chem. Lett.* **2020**, *11*, 8668–8674.
- (31) Tantis, I.; Talande, S.; Tzitzios, V.; Basina, G.; Shrivastav, V.; Bakandritsos, A.; Zboril, R. Non-van der Waals 2D Materials for

- Electrochemical Energy Storage. Adv. Funct. Mater. 2023, 33, 2209360.
- (32) Xiao, X.; Wang, H.; Urbankowski, P.; Gogotsi, Y. Topochemical synthesis of 2D materials. *Chem. Soc. Rev.* **2018**, 47, 8744–8765.
- (33) Lam, D.; Lebedev, D.; Hersam, M. C. Morphotaxy of Layered van der Waals Materials. ACS Nano 2022, 16, 7144–7167.
- (34) Wang, Q.; O'Hare, D. Recent advances in the synthesis and application of layered double hydroxide (LDH) nanosheets. *Chem. Rev.* **2012**, *112*, 4124–4155.
- (35) Fan, G.; Li, F.; Evans, D. G.; Duan, X. Catalytic applications of layered double hydroxides: recent advances and perspectives. *Chem. Soc. Rev.* **2014**, *43*, 7040–7066.
- (36) Xia, D.-c.; Zhou, L.; Qiao, S.; Zhang, Y.; Tang, D.; Liu, J.; Huang, H.; Liu, Y.; Kang, Z. Graphene/Ni-Fe layered double-hydroxide composite as highly active electrocatalyst for water oxidation. *Mater. Res. Bull.* **2016**, *74*, 441–446.
- (37) Wang, Y.; Qiao, M.; Li, Y.; Wang, S. Tuning Surface Electronic Configuration of NiFe LDHs Nanosheets by Introducing Cation Vacancies (Fe or Ni) as Highly Efficient Electrocatalysts for Oxygen Evolution Reaction. *Small* **2018**, *14*, 1800136.
- (38) Cai, X.; Shen, X.; Ma, L.; Ji, Z.; Xu, C.; Yuan, A. Solvothermal synthesis of NiCo-layered double hydroxide nanosheets decorated on rGO sheets for high performance supercapacitor. *Chem. Eng. J.* **2015**, 268, 251–259.
- (39) Qin, K.; Wang, L.; Wen, S.; Diao, L.; Liu, P.; Li, J.; Ma, L.; Shi, C.; Zhong, C.; Hu, W.; et al. Designed synthesis of NiCo-LDH and derived sulfide on heteroatom-doped edge-enriched 3D rivet graphene films for high-performance asymmetric supercapacitor and efficient OER. *J. Mater. Chem. A* **2018**, *6*, 8109–8119.
- (40) Kloprogge, J. T.; Hickey, L.; Frost, R. L. FT-Raman and FT-IR spectroscopic study of synthetic Mg/Zn/Al-hydrotalcites. *J. Raman Spectrosc.* **2004**, *35*, 967–974.
- (41) Sarigamala, K. K.; Shukla, S.; Struck, A.; Saxena, S. Rationally engineered 3D-dendritic cell-like morphologies of LDH nanostructures using graphene-based core-shell structures. *Microsyst. Nanoeng.* **2019**, *5*, 65.
- (42) Siwatch, P.; Sharma, K.; Tripathi, S. Facile synthesis of NiCo₂O₄ quantum dots for asymmetric supercapacitor. *Electrochim. Acta* **2020**, 329, 135084.
- (43) Venkatachalam, V.; Alsalme, A.; Alghamdi, A.; Jayavel, R. Hexagonal-like NiCo₂O₄ nanostructure based high-performance supercapacitor electrodes. *Ionics* **2017**, *23*, 977–984.
- (44) Li, Q.; Lu, C.; Chen, C.; Xie, L.; Liu, Y.; Li, Y.; Kong, Q.; Wang, H. Layered NiCo₂O₄/reduced graphene oxide composite as an advanced electrode for supercapacitor. *Energy Storage Mater.* **2017**, *8*, 59–67.
- (45) Babu, G. A.; Ravi, G.; Hayakawa, Y.; Karaikudi, T. N. K. Surfactant assisted growth and optical studies of $NiCo_2O_4$ nanostructures through microwave heating method. *Int. J. Appl. Sci., Eng.* **2014**, *1*, 17–20.
- (46) Li, D.; Gong, Y.; Wang, M.; Pan, C. Preparation of sandwich-like NiCo₂O₄/rGO/NiO heterostructure on nickel foam for high-performance supercapacitor electrodes. *Nano-Micro Lett.* **2017**, *9*, 16.
- (47) Sahoo, P.; Sahoo, R. C.; Matte, H. S. S. R. Determination of Hansen Solubility Parameter and In Situ Visualization of Dispersion Stability of Solution-Processed Antimonene. *ACS Appl. Nano Mater.* **2023**, *6*, 21957–21966.
- (48) Detloff, T.; Sobisch, T.; Lerche, D. Instability index. *Dispersion Letters Technical* **2013**, *T4*, 1–4.
- (49) Fernandes, A. R.; Ferreira, N. R.; Fangueiro, J. F.; Santos, A. C.; Veiga, F. J.; Cabral, C.; Silva, A. M.; Souto, E. B. Ibuprofen nanocrystals developed by 22 factorial design experiment: A new approach for poorly water-soluble drugs. *Saudi Pharm. J.* **2017**, 25, 1117–1124.
- (50) Brunelli, A.; Zabeo, A.; Semenzin, E.; Hristozov, D.; Marcomini, A. Extrapolated long-term stability of titanium dioxide nanoparticles and multi-walled carbon nanotubes in artificial freshwater. *J. Nanopart. Res.* **2016**, *18*, 113.

- (51) Chiu, H.-T.; Yang, H.-M.; Liu, C.-S.; Hsu, H.-Y. Synthesis, stability and properties of polyurethane/acrylic hybrids using m-TMXDI-based anionic poly (urethane-urea) dispersion. *Polym.-Plast. Technol. Eng.* **2012**, *51*, 945–953.
- (52) Jain, A.; Ong, S. P.; Hautier, G.; Chen, W.; Richards, W. D.; Dacek, S.; Cholia, S.; Gunter, D.; Skinner, D.; Ceder, G.; et al. Commentary: The Materials Project: A materials genome approach to accelerating materials innovation. *APL Mater.* **2013**, *1*, 011002.
- (53) Barnowsky, T.; Krasheninnikov, A. V.; Friedrich, R. A New Group of 2D Non-van der Waals Materials with Ultra Low Exfoliation Energies. *Adv. Electron. Mater.* **2023**, *9*, 2201112.
- (54) Mounet, N.; Gibertini, M.; Schwaller, P.; Campi, D.; Merkys, A.; Marrazzo, A.; Sohier, T.; Castelli, I. E.; Cepellotti, A.; Pizzi, G.; et al. Two-dimensional materials from high-throughput computational exfoliation of experimentally known compounds. *Nat. Nanotechnol.* **2018**, *13*, 246–252.
- (55) Zacharia, R.; Ulbricht, H.; Hertel, T. Interlayer cohesive energy of graphite from thermal desorption of polyaromatic hydrocarbons. *Phys. Rev. B* **2004**, *69*, 155406.
- (56) Friedrich, R.; Ghorbani-Asl, M.; Curtarolo, S.; Krasheninnikov, A. V. Data-driven quest for two-dimensional non-van der Waals materials. *Nano Lett.* **2022**, *22*, 989–997.
- (57) Wang, H.; Gao, Q.; Jiang, L. Facile approach to prepare nickel cobaltite nanowire materials for supercapacitors. *Small* **2011**, *7*, 2454–2459.
- (58) Deokate, R. J.; Kalubarme, R. S.; Park, C.-J.; Lokhande, C. D. Simple synthesis of $NiCo_2O_4$ thin films using spray pyrolysis for electrochemical supercapacitor application: a novel approach. *Electrochim. Acta* **2017**, *224*, 378–385.
- (59) Palanisamy, R.; Karuppiah, D.; Venkatesan, S.; Mani, S.; Kuppusamy, M.; Marimuthu, S.; Karuppanan, A.; Govindaraju, R.; Marimuthu, S.; Rengapillai, S.; et al. High-performance asymmetric supercapacitor fabricated with a novel MoS₂/Fe₂O₃/Graphene composite electrode. *Colloids Interface Sci. Commun.* **2022**, 46, 100573.
- (60) Kurra, N.; Uzun, S.; Valurouthu, G.; Gogotsi, Y. Mapping (Pseudo) Capacitive Charge Storage Dynamics in Titanium Carbide MXene Electrodes in Aqueous Electrolytes Using 3D Bode Analysis. *Energy Storage Mater.* **2021**, *39*, 347–353.
- (61) Ko, J. S.; Lai, C.-H.; Long, J. W.; Rolison, D. R.; Dunn, B.; Nelson Weker, J. Differentiating Double-Layer, Psuedocapacitance, and Battery-like Mechanisms by Analyzing Impedance Measurements in Three Dimensions. *ACS Appl. Mater. Interfaces* **2020**, *12*, 14071–14078.
- (62) Taberna, P.; Simon, P.; Fauvarque, J.-F. Electrochemical characteristics and impedance spectroscopy studies of carbon-carbon supercapacitors. *J. Electrochem. Soc.* **2003**, *150*, A292.
- (63) Kumar, R.; Bag, M. Quantifying Capacitive and Diffusion-Controlled Charge Storage from 3D Bulk to 2D Layered Halide Perovskite-Based Porous Electrodes for Efficient Supercapacitor Applications. *J. Phys. Chem. C* **2021**, *125*, 16946–16954.